Journal of Materials Chemistry C

ROYAL SOCIETY OF CHEMISTRY

PAPER

View Article Online
View Journal | View Issue

Cite this: *J. Mater. Chem. C*, 2020, **8**, 4763

The influence of the terminal acceptor and oligomer length on the photovoltaic properties of A–D–A small molecule donors†

Fernando G. Guijarro,[a] Prateek Malhotra,[b] Gaurav Gupta,[b] Ruben Caballero,[a] Pilar de la Cruz,[a] Rahul Singhal,[c] Ganesh D. Sharma *[b] and Fernando Langa *[a]

Received 10th January 2020,
Accepted 24th February 2020

DOI: 10.1039/d0tc00154f

rsc.li/materials-c

Four new A–D–A small molecules (denoted as **FG1–4**) have been designed and synthesized. The compounds have cyclopentadithiophene-vinylene (CPDTV) oligomers of different lengths as the central donor core linked with different terminal acceptor units (3-ethylrhodanine or dicyanomethylene-3-ethylrhodanine). The effects that conjugation length and terminal acceptor units have on the optical and electrochemical properties were investigated. These small molecules were used as donors in conjunction with $PC_{71}BM$ as an acceptor in the bulk heterojunction active layer for the fabrication of solution-processed organic solar cells. Solvent vapor annealing treatment improved the crystallinity and the interpenetrating networks of donor and acceptor phases for exciton dissociation and charge transfer, thus leading to significant improvements in the overall power conversion efficiency (PCE) of the organic solar cells. The PCE values for the organic solar cells based on the optimized **FG1**:$PC_{71}BM$, **FG2**:$PC_{71}BM$, **FG3**:$PC_{71}BM$ and **FG4**:$PC_{71}BM$ active layer were 5.58%, 6.99%, 7.51% and 8.43%, respectively. These results indicate that an enhancement in the PCE of small molecule organic solar cells can be achieved by an increase in conjugation-length and variation of terminal acceptor units in the molecular backbone of small molecules and optimization of the crystallinity and nanoscale interpenetrating morphology by appropriate solvent vapor annealing treatment.

Introduction

Organic solar cells (OSCs) based on the bulk heterojunction (BHJ) have attracted increased research interest for the conversion of solar energy into electrical energy. This is due to their appealing features, which include low cost of fabrication by the solution processing method, light weight, and transparency.[1–5] The BHJ active layers employed for OSCs consist of binary blends of p-type (donor) and n-type (acceptor) organic semiconductors for the dissociation of excitons generated by the absorption of photons into free charge carriers and their subsequent collection by the electrodes. At present, the reported power conversion efficiencies (PCEs) of OSCs formed by conjugated polymers as donors and a non-fullerene acceptor[6,7] with a single junction and tandem structures are 14–16%[8–15] and 17%,[16] respectively. When compared to conjugated polymers, small molecules (SMs) have numerous advantages and these include well-defined molecular structure, high reproducibility, and easier control of frontier energy levels.[17,18] In recent years a revolution in materials promoted by the multiplicity of molecular design and synthetic procedures has led to enhancements in the PCEs of fullerene-based SM-OSCs, which are now in the range 10–12%,[19–25] and these are gradually approaching those of polymer-based OSCs.[26–28] OSCs with a single BHJ active layer and a large area have recently been reported to show an overall PCE of 12%.[29,30]

In order to achieve high PCE values with OSCs based on SMs, the intrinsic optical and electrochemical properties of the SM donors, *i.e.*, absorption spectra, molecular energy levels, and charge carrier mobilities, must be appropriately adjusted. SM donor materials that contain the π-conjugated acceptor–donor–acceptor (A–π–D–π–A) arrangement, which comprises a central electron-rich core (D) linked to two terminal electron-withdrawing units (A) through a π-linker (either donor or

[a] *Universidad de Castilla-La Mancha, Institute of Nanoscience, Nanotechnology and Molecular Materials (INAMOL), Campus de la Fábrica de Armas, Toledo, Spain. E-mail: Fernando.Langa@uclm.es*
[b] *Department of Physics, The LNM Institute of Information Technology (Deemed University), Rupa ki Nangal, Jamdoli, Jaipur, Rajasthan, 302031, India*
[c] *Department of Physics, MNIT, JLN Marg, Jaipur 302017, India*

† Electronic supplementary information (ESI) available: Experimental procedures for the synthesis of **FG1–4** and precursors, ^1H NMR, ^{13}C NMR, FT-IR and MALDI-TOF spectra, TGA, DSC, absorption and emission plots, electrochemical graphics and theoretical calculations. See DOI: 10.1039/d0tc00154f

acceptor) with strong intramolecular charge transfer (ICT), are currently regarded as the most encouraging design approaches to enlarge the absorption profile and adjust the energy levels and bandgaps.[31–34] Additionally, SM donors with high hole mobilities can provide efficient charge transport with reduced charge recombination within the active layer – a situation that is favorable for improving the J_{SC} and FF values in the OSCs.[35] In general, highly crystalline π-conjugated SMs are expected to form well-ordered assemblies through intermolecular π–π stacking, which in turn allows enhanced charge carrier mobilities in the thin films. The charge carrier mobilities of SMs in thin film can generally be increased by designing highly crystalline π-conjugated SMs through intermolecular π–π stacking. Nevertheless, this feature normally leads to the self-aggregation of SM donors and hence the formation of largely phase-segregated domains in BHJ blends, an effect that tends to cause a substantial loss in photocurrent in the OSC. Therefore, it is still of great interest to obtain ideal SM-based BHJ arrangements that can simultaneously maintain their high crystallinity and appropriate nanoscale morphology to enhance exciton dissociation and charge transport in OSCs.

Oligothiophenes[36] and oligothienylvinylenes[37] have shown very promising photovoltaic properties. 4,4-Dihexyl-4*H*-cyclopenta[2,1-*b*:3,4-*b*′]dithiophene (CPDT) shows interesting semiconducting properties[38] such as high electric conductivities, extended conjugation and low bandgaps. Moreover, the rigid fused ring structure lowers the reorganization energy, a factor that has been shown to have an impact on the mobility of charges in organic semiconductors;[39] in fact, CPDT optimizes the molecular packing through linear π-conjugated backbones in A–π–D–π–A small molecule donors in OSCs.[40] Recently, we described the synthesis of cyclopentadithiophenevinylene (CPDTV) oligomers that display very rich redox chemistry through the stabilization of polycationic states of which radical cations and dications are strong NIR absorbers, with the latter displaying singlet diradicaloid character.[41]

In the work described here four new A–D–A-structured SM donors **FG1–4** (Scheme 1) were designed and synthesized. In these compounds CPDTV was adopted as the central D core and this was linked to two terminal 3-ethylrhodanine (Rd) or dicyanomethylene-3-ethylrhodanine (CNRd) acceptors through different numbers (two or three) of CPDTV units. These SMs exhibit appropriate HOMO and LUMO energy levels and are suitable as donors in conjunction with $PC_{71}BM$ as an acceptor for solution processed BHJ-OSCs. Although it is reported that fullerene derivatives have different isomers and also effect the photovoltaic performance of the resulting OSCs.[42] We have used commercially available $PC_{71}BM$ without further purification and recorded its optical and electrochemical properties and found that these properties were matched well with the reported in the literature.

The OSCs based on as-cast active layers showed moderate overall PCE values but these increased significantly after solvent vapor annealing (SVA) treatment. The increase is mainly due to the increase in J_{SC} and FF and is related to the superior crystallinity and crystalline coherence in the active layer induced by the SVA. Overall PCE values of 5.58%, 6.43%, 7.76% and 8.43% were obtained for the OSCs based on optimized **FG1**:$PC_{71}BM$, **FG2**:$PC_{71}BM$, **FG3**:$PC_{71}BM$ and **FG4**:$PC_{71}BM$ active layers, respectively.

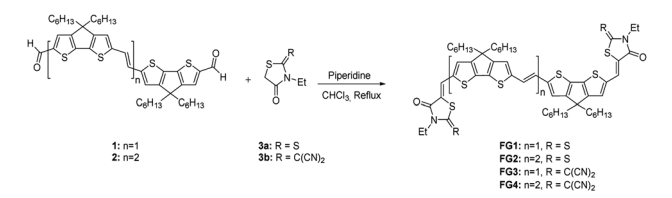

Scheme 1 Synthesis of **FG1–4**.

Results and discussion

Synthesis and characterization

The synthesis of **FG1–4** is depicted in Scheme 1. Bisaldehydes **1** and **2** were prepared according to literature procedures.[41] Knoevenagel condensation between **1** or **2** and 3-ethylrhodanine (**3a**) or dicyanomethylene-3-ethylrhodanine[43] (**3b**), using piperidine as base, afforded compounds **FG1–4** in good yields (50–96%) after purification by column chromatography (silica gel, hexane:$CHCl_3$) and recrystallization (mixture CH_2Cl_2/acetonitrile). All new compounds were characterized by ^{1}H NMR, ^{13}C NMR and FT-IR spectroscopies and by MALDI-MS (see the ESI† for full analytical and spectroscopic data).

The thermal stability of **FG1–4** were studied by thermogravimetric analysis (TGA) and differential scanning calorimetry (DSC) under N_2 atmosphere at 10 K min^{-1} (Fig. S21–S25 in ESI†). All triads showed good thermal stability (weight loss of $<5\%$) up to 280 °C for **FG1**, 327 °C for **FG2**, 342 °C for **FG3** and 333 °C for **FG4**. For each triad an endothermic peak was observed in the DSC curves corresponding to the solid phase transition, implying good crystallinity of **FG1–4** in solid state.

Optical and electrochemical properties

The optical absorption spectra in the UV-vis region of **FG1–4** in benzonitrile solution and thin films are shown in Fig. 1 and the corresponding optical data are compiled in Table 1.

In benzonitrile solution the π–π* transitions are observed at ≈400 nm for the two CPDTV oligomers (**FG1** and **FG3**)

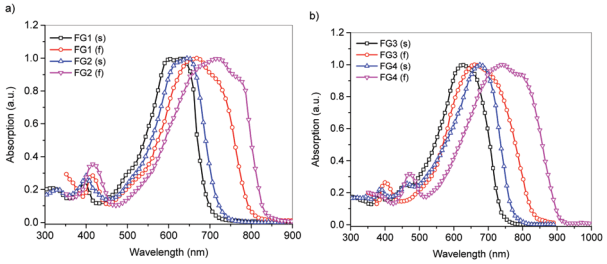

Fig. 1 (a) Normalized absorption spectra of: **FG1** in benzonitrile solution (–) and film (—) and **FG2** in benzonitrile solution (—) and film (—). (b) Normalized absorption spectra of: **FG3** in benzonitrile solution (–) and film (—) and **FG4** in benzonitrile solution (—) and film (—).

Table 1 Optical and redox properties of **FG1–4**

	λ_{abs}/nm (log ε)[a]	λ_{abs}/nm (film)	E^1_{ox}[b] (V)	E^1_{red}[b] (V)	E_{HOMO}[c] (eV)	E_{LUMO}[d] (eV)	E_g[e] (eV)
FG1	405 (4.33) 636 (4.94)	668	0.25	−1.48	−5.35	−3.62	1.73
FG2	474 (4.56) 652 (4.98)	714	0.05	−1.55	−5.15	−3.55	1.60
FG3	415 (4.36) 628 (4.97)	660	0.29	−1.38	−5.39	−3.72	1.67
FG4	484 (4.48) 676 (5.01)	738	0.07	−1.41	−5.17	−3.69	1.48

[a] 10^{-6} M in benzonitrile. [b] Measured by OSWV: 10^{-3} M in ODCB–acetonitrile (4 : 1) *vs.* Fc/Fc$^+$ glassy carbon, Pt counter electrode, 20 °C, 0.1 M Bu_4NClO_4, scan rate = 100 mV s^{-1}. [c] Estimated from $E_{HOMO} = -5.1 - E^1_{ox}$. [d] Estimated from $E_{LUMO} = -5.1 - E^1_{red}$. [e] $E_g = E_{HOMO} - E_{LUMO}$.

and ≈470 nm for the two oligomers with three CPDTV units (**FG2** and **FG4**). **FG1–4** showed intense (log $\varepsilon \approx 5$) and broad absorption bands at around 470–750 nm and these are attributable to an intermolecular charge transfer process between the donor and acceptor units of the small molecules. It was observed that for oligomers **FG3** and **FG4** (with CNRd as acceptor units) there was a bathochromic shift of the absorption maxima by 20–35 nm when compared to **FG1** and **FG2**, which have Rd terminal units, as a consequence of the stronger electron-withdrawing ability of CNRd with respect to Rd. This difference may lead to improved charge transfer. When compared to spectra in solution, the absorption spectra of these SMs in thin film showed red-shifted and broadened ICT absorption bands with the appearance of a vibronic shoulder at longer wavelength for all **FGs**. This change is indicative of molecular aggregation in the solid state. The optical bands, estimated from the absorption edges in the absorption spectra of **FGs** in thin film, are around 1.58 eV, 1.47 eV, 1.50 eV and 1.39 eV for **FG1**, **FG2**, **FG3** and **FG4**, respectively. **FG2** and **FG4**, which have longer conjugation lengths, showed smaller optical bandgaps than **FG1** and **FG3**, respectively. Moreover, the **FGs** with CNRd terminal units showed lower optical bandgaps when compared to the **FGs** with Rd terminal units, a difference that is again attributed to the stronger electron-withdrawing ability of CNRd.[43,44]

Since the HOMO and LUMO energy levels of the SM donors play a crucial role in their application in BHJ OSCs, the energy levels of the **FGs** were determined from the OSWV measurements and are shown in Table 1. As one would expect, an increase in the number of CDT units (or π-conjugation length) gave rise to an increase in the HOMO energy levels from −5.35 eV (**FG1**) to −5.15 eV (**FG2**) and from −5.39 eV (**FG3**) to −5.17 eV (**FG4**). The LUMO energy levels of **FG1**, **FG2**, **FG3** and **FG4** are −3.62 eV, −3.55 eV, −3.72 eV and −3.69 eV, respectively. It can be observed that the terminal CNRd units lowered both HOMO and LUMO energy levels when compared to Rd units. Considering the HOMO (−6.15 eV) and LUMO (−4.15 eV) levels of $PC_{71}BM$, **FG1–4** have appropriate electronic energy levels to act as donors in $PC_{71}BM$-based BHJ OSCs. It is widely reported in the literature that the HOMO and LUMO energy offset between the donor and acceptor must be larger than the exciton binding energy (∼0.1–0.3 eV) for efficient exciton dissociation. In **FG1–4**:$PC_{71}BM$ BHJ active layers the HOMO offset and LUMO offset values are 0.73–0.94 eV and 0.41–0.61 eV, respectively, and these are larger than the threshold value for efficient exciton dissociation and charge transfer from **FG1–4** to $PC_{71}BM$ and *vice versa*.

Theoretical calculations

Theoretical calculations (Gaussian 09) were performed using the DFT/B3LYP/6-31G method in order to ascertain the optimized geometries of **FG1–4**. In all cases the structures were completely planar (Fig. 2) with dihedral angles of less than 0.1°. This planarity improves the π aggregation between the molecules and favors the movement of electrons.

The theoretical calculations also provided information about the contour plots of the frontier molecular orbitals of the oligomers under investigation (**FG1–FG4**). In all cases the HOMO and LUMO are both spread over the whole conjugated system (Fig. 3), thus favoring π-electron delocalization.

As far as the theoretical energy levels of the corresponding molecular orbitals (Fig. 3) are concerned, the band gap decreases as the π-conjugation length increases, either by an increase in the number of monomers or by the presence of the dicyanovinylene groups in the acceptor fragments.

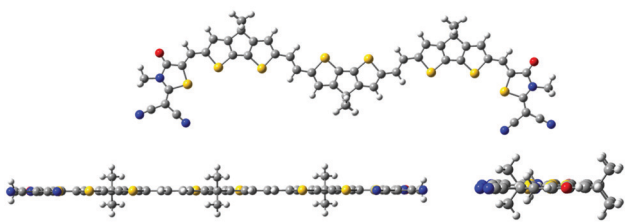

Fig. 2 Theoretical optimized geometry of **FG4**.

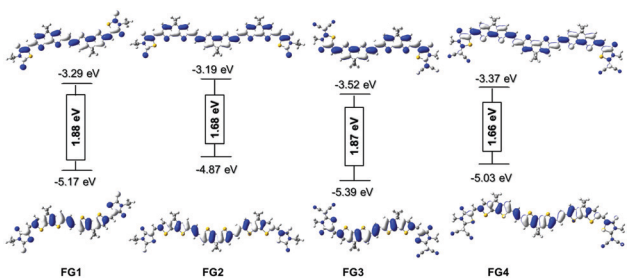

Fig. 3 Theoretically calculated energy levels and electronic contours of the HOMO and LUMO of **FG1**, **FG2**, **FG3** and **FG4**.

The theoretical values obtained for the molecular orbital energies are reasonably consistent with those obtained in the electrochemical studies (Table 1) and the trends in the HOMO–LUMO energy gaps are consistent with the optical bandgap.

The dipole moments calculated from the DFT simulation (see the ESI†) show that **FG4** has the highest value for both the ground state and excited state when compared to the other compounds.

Photovoltaic properties

Solution-processed BHJ OSCs were fabricated and characterized in order to obtain information about the influence that the different backbone structures of the **FG** donors had on the photovoltaic performance in conjunction with the $PC_{71}BM$ acceptor. A conventional device structure of ITO/PEDOT:PSS/**FG1–4**:$PC_{71}BM$/PFN/Al was used (details for the device fabrication and characterization are given in the ESI†). The photovoltaic performance of BHJ OSCs was initially optimized by varying the donor-to-acceptor ratio in benzonitrile as solvent without any additional treatment. It was found that the OSCs fabricated with as-cast (D/A weight ratio of 1 : 1.5) films showed the best photovoltaic performance (Table 2).

It can be seen from the results in Table 2 that the OSCs based on as-cast active layers showed overall PCE values in the range 1.8–3.0% despite the high V_{OC} (0.94 V) for **FG3**. The low PCE values for the OSCs based on as-cast BHJ active layers may due to the poor nanoscale morphology of the active layers, which limits the charge transport and leads to low FF and J_{SC} values.

Solvent vapor annealing (SVA) treatment of the optimized as-cast BHJ active layers was carried out to improve the active layer morphology. Tetrahydrofuran (THF) was used as the annealing solvent because it has a high vapor pressure under atmospheric conditions[45] and it is used for most SM-based OSCs. It was observed that all **FG1–4**:$PC_{71}BM$ BHJ OSCs showed the best PCEs with an SVA duration of 50 s. When the active layer was exposed for more than 50 s a decrease in the overall PCE was observed. It was assumed that the crystallites of **FG** donors grew during the SVA treatment but prolonged SVA led to over-growth of the domains and resulted in a reduction in both the J_{SC} and FF. The current–voltage (J–V) characteristics of the optimized SVA-treated OSCs under illumination (AM 1.5 G, 100 mW cm^{-2}) are shown in Fig. 4a and the photovoltaic parameters are summarized in Table 2. Among the SVA-treated OSCs, the highest PCE of 8.43% with a J_{SC} of 16.38 mA cm^{-2}, V_{OC} of 0.78 V and FF of 0.67 was achieved for the **FG4**:$PC_{71}BM$ BHJ active layer. The V_{OC} of the OSC based on **FG3**:$PC_{71}BM$ was the highest of all the OSCs because of the deepest-lying HOMO energy level of **FG3**, which is caused by the stronger electron-withdrawing CNRd units.

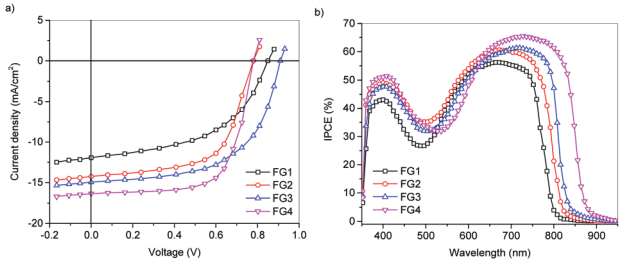

Fig. 4 (a) Current density *versus* voltage characteristics of the devices prepared with **FG1–4** and $PC_{71}BM$ after SVA. (b) IPCE curves for the devices.

The incident photon to current conversion efficiency (IPCE) spectra for the optimized SVA treated OSCs are shown in Fig. 4b. It can be seen that the IPCE spectra of the OSCs have two bands; the band below 500 nm corresponds to the exciton generated due to the photons absorbed by the $PC_{71}BM$ whereas the band above 500 nm corresponds to the exciton generation in the **FGs** phase in the active layer, with both the $PC_{71}BM$ and **FGs** contributing to the photocurrent generation in the OSCs. The J_{SC} values estimated from the integration of the IPCE spectra are 11.82, 14.83, 14.12 and 16.25 mA cm^{-2} for the OSCs based on **FG1**, **FG2**, **FG3** and **FG4**, respectively, and these values are very close to those obtained from the J–V characteristics under illumination.

The effects of the number of CDPTV units and SVA treatment on the charge transport properties were confirmed by evaluating the hole and electron mobilities by the space charge limited current (SCLC) method.[46,47] The hole and electron mobilities (μ_h and μ_e, respectively) determined for **FG1–4**:$PC_{71}BM$ blend films both with and without SVA treatment are presented in Table 3 and the corresponding dark J–V characteristics are presented in Fig. 5a and b.

All of the as-cast blend films exhibited hole mobilities in the range 1.02–5.17 × 10^{-5} cm^2 V^{-1} s^{-1} and after SVA treatment the hole mobility in all of the blends had increased significantly

Table 2 Photovoltaic parameters of **FG1–FG4** based on different active layers

Active layer	J_{SC}	V_{OC} (V)	FF	PCE (%)
FG1:$PC_{71}BM$ (as cast)	6.78	0.89	0.31	1.87 (1.79)[a]
FG2:$PC_{71}BM$ (as cast)	8.32	0.81	0.35	2.36 (2.20)[a]
FG3:$PC_{71}BM$ (as cast)	7.83	0.94	0.34	2.50 (2.43)[a]
FG4:$PC_{71}BM$ (as cast)	9.82	0.81	0.39	3.10 (3.03)[a]
FG1:$PC_{71}BM$ (SVA)	11.92	0.85	0.55	5.57 (5.52)[a]
FG2:$PC_{71}BM$ (SVA)	14.94	0.78	0.60	6.99 (6.84)[a]
FG3:$PC_{71}BM$ (SVA)	14.24	0.91	0.58	7.51 (7.39)[a]
FG4:$PC_{71}BM$ (SVA)	16.38	0.78	0.66	8.43 (8.37)[a]

[a] Average of eight devices.

Table 3 Hole and electron mobilities (μ_h, μ_e) for **FG1–4**:$PC_{71}BM$ blend films

Active layer	μ_h (cm^2 V^{-1} s^{-1})	μ_e (cm^2 V^{-1} s^{-1})	μ_e/μ_h
FG1:$PC_{71}BM$ (as cast)	1.02 × 10^{-5}	2.46 × 10^{-4}	24.11
FG2:$PC_{71}BM$ (as cast)	1.43 × 10^{-5}	2.44 × 10^{-4}	17.06
FG3:$PC_{71}BM$ (as cast)	3.68 × 10^{-5}	2.42 × 10^{-4}	6.58
FG4:$PC_{71}BM$ (as cast)	5.17 × 10^{-5}	2.48 × 10^{-4}	4.80
FG1:$PC_{71}BM$ (SVA)	9.93 × 10^{-5}	2.52 × 10^{-4}	2.54
FG2:$PC_{71}BM$ (SVA)	1.53 × 10^{-4}	2.48 × 10^{-4}	1.62
FG3:$PC_{71}BM$ (SVA)	1.18 × 10^{-4}	2.48 × 10^{-4}	2.10
FG4:$PC_{71}BM$ (SVA)	1.85 × 10^{-4}	2.42 × 10^{-4}	1.31

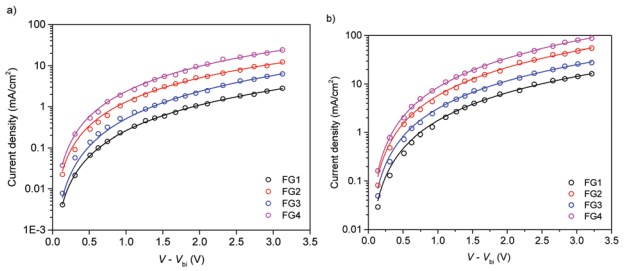

Fig. 5 Dark J–V characteristics of hole-only devices based on (a) as-cast and (b) SVA-treated **FG1**:$PC_{71}BM$, **FG2**:$PC_{71}BM$, **FG3**:$PC_{71}BM$ and **FG4**:$PC_{71}BM$ films.

(to around 10^{-4} cm^2 V^{-1} s^{-1}). Moreover, the hole mobility of **FGs** in the blend also depended on the conjugation length of the molecular backbone and increased with increasing conjugation length (**FGs** with 3CPDTV had higher hole mobility than **FGs** with 2CPDTV). The hole mobilities for **FG2** and **FG4** were higher than those for **FG1** and **FG3** (both as-cast and SVA treated) and this trend can be attributed to the higher degree of molecular ordering caused by the cyano groups of RdCN within the SVA-treated blend films. In contrast, the electron mobility for the **FG1–4**:$PC_{71}BM$ blend films did not change significantly after SVA treatment (see Table 3). Moreover, the ratio of electron/hole mobility was lower for the **FG** blends having 3CDPTV units as compared to the 2CPDTV counterpart. The reduction in the electron to hole mobility ratio indicates more balanced charge transport in the OSCs based on SVA-treated **FG3** and **FG4** and this resulted in higher FF values for the corresponding OSCs.[48]

Both the J_{SC} and FF values for the OSCs based on the SVA-treated active layers are higher than those of the as-cast active layers. This result is related to the suppressed charge recombination losses. The J_{SC} and FF values are also related to the variation in the electron-accepting ability of the terminal units and the conjugation length of the molecular backbone (number of CPDTV units). Therefore, the charge recombination mechanism was analyzed through the variation of V_{OC} and J_{SC} with illumination intensity (P_{in}) and the results are represented in Fig. 6a and b, respectively (SVA-treated active layer). The light intensity dependence of V_{OC} with P_{in} was fitted to the linear law $V_{OC} \propto (nkT/q)\ln(P_{in})$, where k, T and q are Boltzmann's constant, temperature in Kelvin and elementary charge, respectively. On the basis of diode theory, the value of n should lie in the range 1–2 and n values greater than unity are attributed to more trap-assisted recombination in the device.[49] The n values for the OSCs based on as-cast active layers are above 1.50, which is consistent with the interior performance of these OSCs and may be related to more trap-assisted surface recombination.[7] The n values for the SVA-treated OSCs were 1.35, 1.28, 1.22 and 1.17 for **FG1**, **FG2**, **FG3** and **FG4**, respectively. This decrease in the n value indicates that trap-assisted recombination is suppressed upon increasing the conjugation length and the electron accepting ability of the terminal units – a finding that corresponds well with the high FF valves. As shown in Fig. 6a, the relationship between J_{SC} and P_{in} can be described as $J_{SC} \propto (P_{in})^{\alpha}$ and the α values for as-cast active layers of **FG1**, **FG2**, **FG3** and **FG4** are 0.793, 0.831, 0.814 and 0.847, respectively, which suggests that these devices suffer from marked bimolecular recombination and this is one of the main reasons for the very low FF values. The value of α increased to 0.932, 0.948, 0.959 and 0.969 for OSCs based on SVA-treated **FG1**:$PC_{71}BM$, **FG2**:$PC_{71}BM$, **FG3**:$PC_{71}BM$ and **FG4**:$PC_{71}BM$, respectively. This indicates that bimolecular recombination is suppressed effectively, which in turn leads to an improvement in the FF values.[50] Moreover, the α value for the **FG2**-based OSC is higher than those for **FG1** and **FG4**, which in turn are higher than that for **FG3** processed under identical conditions. This trend indicates that the conjugation length and the electron-accepting ability of the terminal units also play important roles in the charge recombination processes. The conjugation length of the molecular backbone and higher electron-accepting capability of the terminal units effectively suppresses the bimolecular recombination.

The charge collection and exciton dissociation mechanism in the active layers were also investigated and the corresponding photocurrent density (J_{ph})–effective voltage (V_{eff}) curves[51] of the optimized (SVA-treated) devices are shown in Fig. 7a and b for as-cast and SVA-treated active layers. J_{ph} was estimated as $J_L - J_D$, where J_L and J_D are the current densities under illumination and in the dark, respectively, V_{eff} is defined as $V_0 - V$, where V_0 is the voltage at which $J_{ph} = 0$ and V is the applied voltage. It can be seen from Fig. 7a that for the OSCs based on as-cast active layers, J_{ph} shows a strong dependence on V_{eff} and J_{ph} continuously increases with V_{eff} and does not saturate even at the highest V_{eff} value. This behaviour indicates a significant problem in the charge extraction, and this leads to very low FF values. However, in the case of OSCs based on

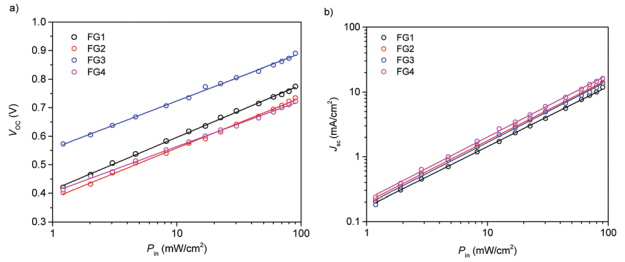

Fig. 6 Variation of (a) V_{OC} and (b) J_{SC} with illumination intensity (P_{in}) for OSCs based on SVA-treated **FG1**:$PC_{71}BM$, **FG2**:$PC_{71}BM$, **FG3**:$PC_{71}BM$, and **FG4**:$PC_{71}BM$ films.

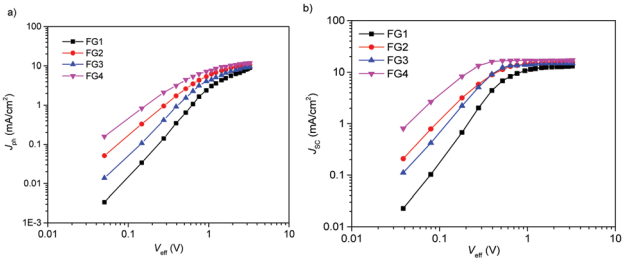

Fig. 7 Variation of photocurrent density (J_{ph}) with effective voltage (V_{eff}) for OSCs based on (a) as-cast and (b) SVA-treated **FG1**:$PC_{71}BM$, **FG2**:$PC_{71}BM$, **FG3**:$PC_{71}BM$ and **FG4**:$PC_{71}BM$ films.

SVA-treated active layers (Fig. 7b), J_{ph} increases sharply with increasing V_{eff} and immediately tends to saturate. The exciton dissociation probability (P_{diss}) and charge collection probability (P_{coll}) values were estimated from the ratio of J_{ph}/J_{phsat} at short circuit conditions and maximum power point, respectively. The P_{diss}/P_{coll} values for the OSCs based on as-cast **FG1**, **FG2**, **FG3** and **FG4** are 0.75/0.52, 0.806/0.582, 0.775/0.563 and 0.826/0.621, respectively, and the low P_{diss} is consistent with the low FF and J_{SC} values for as-cast OSCs and may be attributed to charge recombination. However, the P_{diss}/P_{coll} values for the SVA-treated OSCs based on **FG1**, **FG2**, **FG3** and **FG4** are 0.912/0.734, 0.951/0.744, 0.928/0.744 and 0.965/0.785, respectively, *i.e.*, higher than for the as-cast counterparts, which indicates that that exciton dissociation into free charge carriers and subsequent charge collection are improved after the SVA treatment. Moreover, the P_{diss}/P_{coll} values for the OSCs based on 3CPDTV are higher than those for 2CPDTV and they are also higher for the CNRd when compared to the Rd counterpart. These observations indicate that exciton dissociation and charge collection also improved with longer conjugation length and stronger electron-accepting terminal units in the **FGs**, thus leading to the highest FF value for **FG4**. The lowest charge recombination and highest P_{diss}/P_{coll} value for the **FG4**-based OSC implies that this device had efficient charge dissociation and charge collection. It can be seen from J_{ph}–V_{eff} characteristics that J_{ph} is independent of V_{eff} and that J_{ph} is controlled only by the light-harvesting efficiency of the active layer. The maximum exciton generation rate G_{max} can be estimated as $G_{max} = J_{phsat}/qL$, where q is the electronic charge and L is the thickness of the active layer. The G_{max} values for the OSCs based on optimized active layers with **FG1**:$PC_{71}BM$, **FG2**:$PC_{71}BM$, **FG3**:$PC_{71}BM$ and **FG4**:$PC_{71}BM$ are around 0.98×10^{28} m^{-3} s^{-1}, 1.13×10^{28} m^{-3} cm^{-1}, 1.08×10^{28} m^{-3} s^{-1} and 1.24×10^{28} m^{-3} s^{-1}, respectively, and these values are consistent with the absorption profiles of these **FGs**.

X-ray diffraction (XRD) measurements were employed to provide additional information on the effect of SVA treatment on the molecular ordering and crystallinity within the active layers. The pattern for **FG4**:$PC_{71}BM$ as a representative example is provided in Fig. 8. Similar XRD patterns were observed for other active layers. In as-cast blend films, weak (100) reflections originating from the lamellar structures of **FG1–4** were observed in the range 2θ = 4.56–4.92 with a d_{100} spacing of 1.97–1.82 nm. In addition to the afore mentioned (100) reflection, very weak (010) diffraction peaks were observed in the range 2θ = 22.06–22.78 with a π–π stacking distance of 0.41–0.393 nm. After SVA treatment the intensity of both the (100) and (010) diffraction peaks increased significantly and this can be attributed to enhanced molecular ordering and crystallinity. The (010) diffraction peak for the SVA-treated blend was shifted to a higher 2θ value (23.05–23.76, with π–π stacking distances in the range 0.393–0.382 nm), which is beneficial for charge transport. The π–π stacking reflection was more pronounced in **FG3** and **FG4** and the π–π stacking distances in **FG3** and **FG4** are slightly shorter than those in **FG1** and **FG2**, thus implying the existence of stronger intermolecular interactions in the **FGs** with CNRd terminal units – a situation that is beneficial for charge transport. Therefore, it can be concluded that appropriate SVA treatment is highly effective for **FG1–4** to induce molecular order and crystallinity as well as to achieve better nanoscale phase separation between **FG1–4** and $PC_{71}BM$, with more crystalline domains present in the BHJ active layers. These effects ultimately lead to enhanced charge transport and higher overall PCEs for the OSCs.[44]

Moreover, we have measured the transmission electron microscope (TEM) images of the optimized active layers and shown in Fig. S39, ESI.† All the TEM images exhibits bright and dark domains attributed to the donor and acceptor due to their different electron densities.[52] The active layer based on FG4:$PC_{71}BM$ showed the largest domain size (better interpenetrating pathways for electron and hole transportation) and FG1:$PC_{71}BM$ showed the smallest domain size. The better interpenetrating phase separation is beneficial for the high value of J_{SC} and FF.

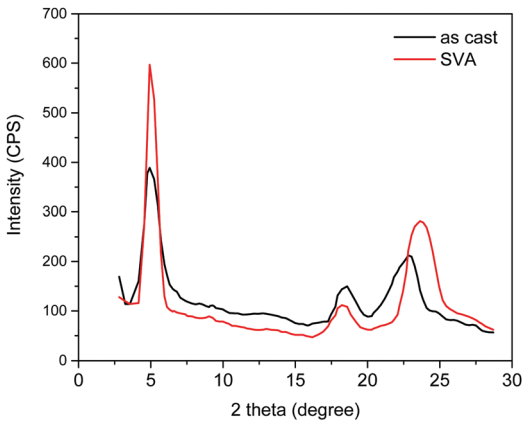

Fig. 8 XRD patterns of as-cast (black) and SVA-treated (red) **FG4**:$PC_{71}BM$ thin films.

Conclusions

Four new A–D–A small molecules (**FG1–4**) with CPDTV as a donor unit and Rd or CNRd as terminal electron-withdrawing units were synthesized. The optical and electrochemical properties of these new materials were investigated. The **FGs** had encouraging optical and electrochemical properties for use as donor materials in conjunction with $PC_{71}BM$ as the acceptor in solution-processed BHJ OSCs. The OSCs based on as-cast BHJ active layers showed overall PCE values in the range 1.8–3.0%, mainly due to the low J_{SC} and FF values, which are related to poor molecular ordering and crystallinity in the active layer and poor charge transport due to unbalanced charge carrier mobilities. SVA treatment of the active layers using THF as the annealing solvent led to significantly enhanced PCE values for the BHJ OSCs based on **FG1–4**:$PC_{71}BM$. Appropriate SVA treatment (50 s) led to improvements in the PCE values up to 5.58%, 6.99%, 7.51% and 8.43% for **FG1**, **FG2**, **FG3** and **FG4** OSCs, respectively. The increase in the PCE of OSCs based on SVA-treated active layers is mainly related to the improved J_{SC}

and FF values. These improvements are attributed to controlled molecular ordering, appropriate nanoscale morphology and interpenetrating network for efficient exciton dissociation and charge collection, and a reduction in bimolecular recombination and trap-assisted recombination. These aspects were investigated by XRD, SCLC measurements and the dependence of photocurrent and photovoltage on illumination intensities. The overall PCE values of OSCs based on the **FGs** containing CNRd were higher than those for **FGs** based on Rd. This trend may be related to existence of strong intermolecular interactions in the CNRd-based **FG** donors. The PCE of SMs based on 3-CPDTV were higher than for 2-CPDTV-based counterparts and this indicates that the longer conjugation length is beneficial for increased molecular ordering and crystallinity and favorable for exciton dissociation and charge transport. These studies offer valuable information about the structure–property relationships for OSCs based on small molecules and could provide an effective design strategy for the further development of high-performance CPDT-based SMs and OSCs.

Conflicts of interest

There are no conflicts to declare.

Acknowledgements

F. L. and P. C. thank MINECO (Spain) (CTQ2016-79189-R) and the Junta de Comunidades de Castilla-La Mancha and European Social Fund (SBPLY/17/180501/000254) for financial support. F. G. thanks the Junta de Comunidades de Castilla-la Mancha for an FPI grant (SBPLY/16/180501/000504). Prof. G. D. S. thanks the Department of Science and Technology (Government of India) (DST/TMD/SERI/D05 C) for financial support.

References

1 G. Li, R. Zhu and Y. Yang, *Nat. Photonics*, 2012, **6**, 153–161.
2 L. Dou, J. You, Z. Hong, Z. Xu, G. Li, R. A. Street and Y. Yang, *Adv. Mater.*, 2013, **25**, 6642–6671.
3 F. C. Krebs, N. Espinosa, M. Hösel, R. R. Søndergaard and M. Jørgensen, *Adv. Mater.*, 2014, **26**, 29–39.
4 Y. Huang, E. J. Kramer, A. J. Heeger and G. C. Bazan, *Chem. Rev.*, 2014, **114**, 7006–7043.
5 L. Lu, T. Zheng, Q. Wu, A. M. Schneider, D. Zhao and L. Yu, *Chem. Rev.*, 2015, **115**, 12666–12731.
6 J. Hou, O. Inganäs, R. H. Friend and F. Gao, *Nat. Mater.*, 2018, **17**, 119–128.
7 G. Zhang, J. Zhao, P. C. Y. Chow, K. Jiang, J. Zhang, Z. Zhu, J. Zhang, F. Huang and H. Yan, *Chem. Rev.*, 2018, **118**, 3447–3507.
8 S. Li, L. Ye, W. Zhao, H. Yan, B. Yang, D. Liu, W. Li, H. Ade and J. Hou, *J. Am. Chem. Soc.*, 2018, **140**, 7159–7167.
9 W. Zhao, S. Li, H. Yao, S. Zhang, Y. Zhang, B. Yang and J. Hou, *J. Am. Chem. Soc.*, 2017, **139**, 7148–7151.
10 H. Zhang, H. Yao, J. Hou, J. Zhu, J. Zhang, W. Li, R. Yu, B. Gao, S. Zhang and J. Hou, *Adv. Mater.*, 2018, **30**, 1800613.
11 Y. Cui, H. Yao, L. Hong, T. Zhang, Y. Xu, K. Xian, B. Gao, J. Qin, J. Zhang, Z. Wei and J. Hou, *Adv. Mater.*, 2019, **31**, 1808356.
12 B. Fan, D. Zhang, M. Li, W. Zhong, Z. Zeng, L. Ying, F. Huang and Y. Cao, *Sci. China: Chem.*, 2019, **62**, 746–752.
13 J. Yuan, Y. Zhang, L. Zhou, G. Zhang, H.-L. Yip, T.-K. Lau, X. Lu, C. Zhu, H. Peng, P. A. Johnson, M. Leclerc, Y. Cao, J. Ulanski, Y. Li and Y. Zou, *Joule*, 2019, **3**, 1140–1151.
14 X. Xu, K. Feng, Z. Bi, W. Ma, G. Zhang and Q. Peng, *Adv. Mater.*, 2019, **31**, 1901872.
15 X. Xu, K. Feng, Y. W. Lee, H. Y. Woo, G. Zhang and Q. Peng, *Adv. Funct. Mater.*, 2020, 1907570.
16 L. Meng, Y. Zhang, X. Wan, C. Li, X. Zhang, Y. Wang, X. Ke, Z. Xiao, L. Ding, R. Xia, H. L. Yip, Y. Cao and Y. Chen, *Science*, 2018, **361**, 1094–1098.
17 R. Ilmi, A. Haque and M. S. Khan, *Org. Electron.*, 2018, **58**, 53–62.
18 X. He, L. Yin and Y. Li, *J. Mater. Chem. C*, 2019, **7**, 2487–2521.
19 D. Deng, Y. Zhang, J. Zhang, Z. Wang, L. Zhu, J. Fang, B. Xia, Z. Wang, K. Lu, W. Ma and Z. Wei, *Nat. Commun.*, 2016, **7**, 13740.
20 B. Kan, M. Li, Q. Zhang, F. Liu, X. Wan, Y. Wang, W. Ni, G. Long, X. Yang, H. Feng, Y. Zuo, M. Zhang, F. Huang, Y. Cao, T. P. Russell and Y. Chen, *J. Am. Chem. Soc.*, 2015, **137**, 3886–3893.
21 B. Kan, Q. Zhang, M. Li, X. Wan, W. Ni, G. Long, Y. Wang, X. Yang, H. Feng and Y. Chen, *J. Am. Chem. Soc.*, 2014, **136**, 15529–15532.
22 Y. Liu, C.-C. Chen, Z. Hong, J. Gao, Y. M. Yang, H. Zhou, L. Dou, G. Li, Y. M. Yang, Y. (Michael) Yang, H. Zhou, L. Dou, G. Li and Y. M. Yang, *Sci. Rep.*, 2013, **3**, 3356.
23 J. Wan, X. Xu, G. Zhang, Y. Li, K. Feng and Q. Peng, *Energy Environ. Sci.*, 2017, **10**, 1739–1745.
24 L. Nian, K. Gao, Y. Jiang, Q. Rong, X. Hu, D. Yuan, F. Liu, X. Peng, T. P. Russell and G. Zhou, *Adv. Mater.*, 2017, 1700616.
25 K. Gao, S. B. Jo, X. Shi, L. Nian, M. Zhang, Y. Kan, F. Lin, B. Kan, B. Xu, Q. Rong, L. Shui, F. Liu, X. Peng, G. Zhou, Y. Cao and A. K.-Y. Jen, *Adv. Mater.*, 2019, **31**, 1807842.
26 J. Zhao, Y. Li, G. Yang, K. Jiang, H. Lin, H. Ade, W. Ma and H. Yan, *Nat. Energy*, 2016, **1**, 15027.
27 Z. He, B. Xiao, F. Liu, H. Wu, Y. Yang, S. Xiao, C. Wang, T. P. Russell and Y. Cao, *Nat. Photonics*, 2015, **9**, 174–179.
28 H. Li, D. He, P. Mao, Y. Wei, L. Ding and J. Wang, *Adv. Energy Mater.*, 2017, **7**, 1602663.
29 B. Fan, X. Du, F. Liu, W. Zhong, L. Ying, R. Xie, X. Tang, K. An, J. Xin, N. Li, W. Ma, C. J. Brabec, F. Huang and Y. Cao, *Nat. Energy*, 2018, **3**, 1051–1058.
30 Q. Kang, L. Ye, B. Xu, C. An, S. J. Stuard, S. Zhang, H. Yao, H. Ade and J. Hou, *Joule*, 2019, **3**, 227–239.
31 J. Zhou, X. Wan, Y. Liu, Y. Zuo, Z. Li, G. He, G. Long, W. Ni, C. Li, X. Su and Y. Chen, *J. Am. Chem. Soc.*, 2012, **134**, 16345–16351.

32 J. Zhou, Y. Zuo, X. Wan, G. Long, Q. Zhang, W. Ni, Y. Liu, Z. Li, G. He, C. Li, B. Kan, M. Li and Y. Chen, *J. Am. Chem. Soc.*, 2013, **135**, 10–13.
33 A. Tang, C. Zhan and J. Yao, *Chem. Mater.*, 2015, **27**, 4719–4730.
34 H. Komiyama, T. To, S. Furukawa, Y. Hidaka, W. Shin, T. Ichikawa, R. Arai and T. Yasuda, *ACS Appl. Mater. Interfaces*, 2018, **10**, 11083–11093.
35 M.-H. Jao, H.-C. Liao and W.-F. Su, *J. Mater. Chem. A*, 2016, **4**, 5784–5801.
36 A. Mishra, T. Rana, A. Looser, M. Stolte, F. Würthner, P. Bäuerle and G. D. Sharma, *J. Mater. Chem. A*, 2016, **4**, 17344–17353.
37 N. F. Montcada, B. Pelado, A. Viterisi, J. Albero, J. Coro, P. de la Cruz, F. Langa and E. Palomares, *Org. Electron.*, 2013, **14**, 2826–2832.
38 P. Coppo and M. L. Turner, *J. Mater. Chem.*, 2005, **15**, 1123–1133.
39 J. L. Brédas, J. P. Calbert, D. A. da Silva Filho and J. Cornil, *Proc. Natl. Acad. Sci. U. S. A.*, 2002, **99**, 5804 LP–5809.
40 S. Arrechea, A. Aljarilla, P. de la Cruz, M. K. Singh, G. D. Sharma and F. Langa, *J. Mater. Chem. C*, 2017, **5**, 4742–4751.
41 P. Mayorga Burrezo, R. Domínguez, J. L. Zafra, T. M. Pappenfus, P. de la Cruz, L. Welte, D. E. Janzen, J. T. López Navarrete, F. Langa and J. Casado, *Chem. Sci.*, 2017, **8**, 8106–8114.
42 T. Umeyama and H. Imahori, *Acc. Chem. Res.*, 2019, **52**, 2046–2055.
43 Q. Zhang, B. Kan, F. Liu, G. Long, X. Wan, X. Chen, Y. Zuo, W. Ni, H. Zhang, M. Li, Z. Hu, F. Huang, Y. Cao, Z. Liang, M. Zhang, T. P. Russell and Y. Chen, *Nat. Photonics*, 2014, **9**, 35.
44 S. Furukawa, H. Komiyama, N. Aizawa and T. Yasuda, *ACS Appl. Mater. Interfaces*, 2018, **10**, 42756–42765.
45 K. Sun, Z. Xiao, E. Hanssen, M. F. G. Klein, H. H. Dam, M. Pfaff, D. Gerthsen, W. W. H. Wong and D. J. Jones, *J. Mater. Chem. A*, 2014, **2**, 9048–9054.
46 C. Ramasastry, Y. V. G. S. Murti and B. S. V. S. R. Acharyulu, in *Electrical Transport in Ionic Crystals*, ed. C. N. R. Rao, Modern Aspects of Solid State Chemistry, Springer US, Boston, MA, 1970, pp. 377–390.
47 P. W. M. Blom, M. J. M. de Jong and J. J. M. Vleggaar, *Appl. Phys. Lett.*, 1996, **68**, 3308–3310.
48 P. Zhou, D. Dang, Q. Wang, X. Duan, M. Xiao, Q. Tao, H. Tan, R. Yang and W. Zhu, *J. Mater. Chem. A*, 2015, **3**, 13568–13576.
49 L. J. A. Koster, V. D. Mihailetchi, H. Xie and P. W. M. Blom, *Appl. Phys. Lett.*, 2005, **87**, 203502.
50 Z. Li, J. D. A. Lin, H. Phan, A. Sharenko, C. M. Proctor, P. Zalar, Z. Chen, A. Facchetti and T.-Q. Nguyen, *Adv. Funct. Mater.*, 2014, **24**, 6989–6998.
51 X. Xu, Z. Li, Z. Bi, T. Yu, W. Ma, K. Feng, Y. Li and Q. Peng, *Adv. Mater.*, 2018, **30**, 1800737.
52 S. Zeng, H. Qi, B. Yu, X. Ma, M. Zhang, J. Wang and F. Zhang, *ACS Omega*, 2018, **3**, 11562–11568.

